



Research paper

One-step activation towards spontaneous etching of hollow and hierarchical porous carbon nanospheres for enhanced pollutant adsorption and energy storage

Serene Wen Ling Ng^a, Gamze Yilmaz^{a,b}, Wei Li Ong^a, Ghim Wei Ho^{a,c,d,*}^a Department of Electrical and Computer Engineering, National University of Singapore, 4 Engineering Drive 3, 117583, Singapore^b Department of Chemical and Biomolecular Engineering, National University of Singapore, 4 Engineering Drive 4, 117585, Singapore^c Institute of Materials Research and Engineering, A*STAR (Agency for Science, Technology and Research), 3 Research Link, 117602, Singapore^d Engineering Science Programme, National University of Singapore, 9 Engineering Drive 1, 117575, Singapore

ARTICLE INFO

Keywords:

Carbon
Simultaneous activation-excavation
Hierarchical pores
Hollow and hierarchical pores
VOCs removal
Energy storage

ABSTRACT

Traditionally, porous carbon can be realized through chemical activation as well as templating with different materials for generation of hierarchical pores. However, the former method often results in the loss of the carbon's initial structure, while the latter is known to be complex and requires additional procedures to remove the templates. This work demonstrates one-step activation-excavation approach towards simultaneous etching of hierarchical pores with the preservation of its hollow framework for enhanced volatile organic compounds (VOCs) adsorption and supercapacitance performance. The improvement in activity in both applications stems from the micropores, mesopores and hollow interior for containment, selectivity of larger adsorbents and enhanced transport diffusion respectively for VOCs adsorption. Similarly, the hierarchical pore sizes and hollow cavity in supercapacitors serve the purpose of increased electroactive sites, provides shorter diffusion pathway and facilitates ion diffusion for improved capacitive rate. Thus, this facile and effective approach of producing hollow interior and hierarchical pores carbon nanostructures is promising for bifunctional pollutant removal and energy storage solutions.

1. Introduction

Porous carbon materials have attracted considerable attention due to their many different applications such as water remediation and energy storage [1,2]. Porous carbon has also been adopted as volatile organic compounds (VOCs) adsorbents for removal of toxic pollutants [3,4], catalyst supports [5] as well as electrode materials for electrical double-layer capacitors [6,7]. Furthermore, two-dimensional carbon material such as graphene with hierarchically multimodal pore-size distributions for electrooxidations has also become a hot topic of interest [8–10]. The high demand of porous carbon in the above-mentioned applications is attributed to its intrinsic properties such as high surface area, light-weight, low cost of the material, as well as the ease of obtaining various pore sizes [11]. Hierarchical pore structures, which consists of micro (< 2 nm), meso (2 nm – 50 nm) and macro (> 50 nm) pores, are especially beneficial to VOCs adsorption. Micropores are effective in the containment of VOCs while mesopores provides selectivity especially to adsorption of larger VOCs molecules and accelerates VOCs adsorption [12–15]. A hollow interior (macropores) has a

high surface to volume ratio leading enhanced transport diffusion, thereby improving the surface adsorption of VOCs. [16,17] In addition, a regularly shaped pore structure aids in decreasing the diffusion resistance of adsorbate molecules, thereby reducing the amount of time needed to adsorb the VOCs [12,18]. Similarly, the hierarchical pore structure is also favorable for enhanced supercapacitor performance as the micropores introduce abundant electroactive sites which are essential for high energy storage. Mesopores can be easily and rapidly accessed by electrolyte ions through porous channels, offering shorter diffusion pathways [19]. Moreover, the hollow interior (macropores) serves as ion-buffering reservoirs can effectively accommodate large number of ions, thus increasing the rate capability of the electrode [20]. As a result, synthesizing a hollow, hierarchical pore structures with regularly shaped pores is mandatory for superior performance of VOCs adsorption and supercapacitance.

In recent years, common methods of synthesizing porous carbon include chemical activation through the use of agents such as H₃PO₄, ZnCl₂ and KOH [21–23] and different templating methods such as hard templating with SiO₂, metallic templating or soft templating with

* Corresponding author at: Department of Electrical and Computer Engineering, National University of Singapore, 4 Engineering Drive 3, 117583, Singapore.
E-mail address: elehgw@nus.edu.sg (G.W. Ho).

surfactants [24–29]. The former methods result in structure containing both micropores and mesopores, however, the fundamental spherical structure of the carbon is often lost in the process of activation, leaving no room for the development of a hollow structure [6,21]. At the same time, maintaining regular pores shape might also be difficult due to the inconsistent etching of the carbon material [6]. The latter methods, on the contrary, allow the formation of hollow structure. However, such methods are known to be complicated and often involve the subsequent removal/etching of the core to obtain the required hollow structures [24–29]. As such, simultaneous etching of hierarchical pores with the preservation of its overall hollow frame structure remains particularly challenging stemming from the difficulty in identifying etchant with appropriate attrition capabilities.

Herein, this work presents an easy route using one-step chemical activation to simultaneously generate a hollow cavity and hierarchical pores structure for enhanced pollutant adsorption and energy storage. To the best of our knowledge, this is the first synthesis that demonstrates a convenient way towards readily controllable hierarchical pores and cavity of a carbonaceous material. Compared to other preparation methods, not only does this simple activation-excavation approach creates hierarchical pore sizes and hollow structure, the spherical structure of carbon spheres is not compromised, allowing it to act as a befitting scaffold for subsequent growth of heterostructure for enhanced VOCs degradation. As a proof of concept, the constructed carbon structure has exhibited superior VOCs adsorption due to presences of micro and mesopores, which contain and increase selectivity of adsorption of larger VOCs molecules respectively, while the hollow interior (macropores) promotes transport diffusion of VOCs. Supercapacitance measurements have also revealed superior or comparable capacitive performances compared to recent carbonaceous materials as the hierarchical porous channels act as electroactive sites, provides shorter diffusion pathway while the hollow structure facilitates ion diffusion. In addition, growth of TiO₂ nanosheets on the synthesized carbon leading to improved photocatalytic degradation has also been demonstrated. These findings may open a new straightforward avenue for the design and tailoring of highly porous, well-defined hierarchical and hollow carbon nanostructured materials promising for energy and environmental applications.

2. Experimental methods

2.1. Synthesis of resorcinol formaldehyde (RF)-resin spheres

20 ml of deionized (DI) water was added into 8 ml of pure ethanol (Merck) and stirred at 500 rpm for 10 s. Following which, 0.15 g of resorcinol (Acros Organics) and 0.1 ml of ammonia (Acros Organics) was added to the above solution and left to stir until complete dissolution. 0.21 ml of formaldehyde (Sigma Aldrich) was then added and the solution was left to stir for 24 h. The mixture was transferred to the Teflon-lined autoclave with a capacity of 50 ml and heated at 100 °C for 24 h. The precipitate obtained was washed three times with DI water followed by one time with ethanol via centrifuging. The resulting product was eventually dried at 60 °C and collected for further use.

2.2. Synthesis of activated carbon spheres (ACs)

0.1 g of the as-prepared RF-resin spheres was added to different mass of potassium hydroxide (KOH, Acros Organics). Carbon nanospheres (CNs) were obtained without adding KOH and annealed at 600 °C in a N₂ gas environment with a ramping rate of 5 °C min⁻¹. Porous carbon nanospheres (PCNs) and hollow carbon nanospheres (HCNs) structures were obtained by adding 0.1 g and 0.15 g of KOH respectively and annealed at the same temperature conditions as CNs. After annealing, the powder was washed several times with DI water until the pH reached ~7. The product was dried at 60 °C and collected for further use.

2.3. Synthesis of AC@TiO₂ sheets

5 mg of the as-prepared CNs, PCNs or HCNs were each added to 20 ml of pure ethanol (Merck), followed by 200 µl of diethylenetriamine (DETA, Alfa Aesar) and 40 µl of titanium tetraisopropoxide (TTIP, Sigma Aldrich). The mixture was left to sonicate and stir for 5 min. The solution was then transferred to a Teflon-lined autoclave with a capacity of 50 ml and heated at 200 °C for 20 h. The product was washed three times with ethanol, then eventually dried at 60 °C and annealed at 450 °C for 2 h in a N₂ gas environment with a ramping rate of 2 °C min⁻¹.

2.4. Materials characterization

The scanning electron microscopy (SEM) characterization was carried out using a JEOL FEG JSM 7001F field-emission operating at 15 kV. The EDX characterization was performed with an Oxford Instruments Energy Dispersive X-ray (EDX) System. The crystalline structures were analyzed using transmission electron microscopy (TEM, FEI Tecnai F20X-TWIN) operated at 200 kV and X-ray diffraction (XRD, D5005 Bruker X-ray diffractometer equipped with graphite-monochromated Cu K α radiation at $\lambda = 1.541 \text{ \AA}$). Raman measurements were measured using a microscope (WITecCRM200) with 532 nm (2.33 eV) excitation wavelength and laser power below 0.3 mW. Fourier transform infrared (FTIR) spectra of the products were recorded on a Shimadzu IRPrestige-21 FT-IR spectrophotometer. Brunauer–Emmett–Teller (BET) measurements were conducted using Quantachrome Nova 2200e with N₂ as the adsorbate at liquid nitrogen temperature. The specific surface area (S_{BET}) was calculated according to the multiple-point Brunauer–Emmett–Teller (BET) method at relative pressure $P/P_0 = 0.01\text{--}0.1$. Porosity distributions were calculated by the Quenched Solid Density Functional Theory (QSDFT) and Barrett–Joyner–Halenda (BJH) method. The total pore volume was obtained from the volume of N₂ adsorbed at a relative pressure of $P/P_0 \approx 0.99$. The concentration of VOCs was measured by gas chromatography mass spectrometry (Shimadzu GCMS-QP2010 Ultra). Time-resolved photoluminescence measurement was performed upon excitation of 350 nm fs pulses with average power of 5 mW. The measurement was employed with a mode-locked Ti:sapphire laser (Chameleon Ultra II, Coherent) working at repetition rate of 80 MHz and pulse duration of 140 fs. The second harmonic generation of 700 nm output from the laser was employed to excite the samples. The photoluminescence of the samples was filtered by a 500 nm long pass filter and collected and the PL spectra were detected by a CCD (Princeton Instrument, PIXIS100). The time-resolved PL was performed by using a photon-counting photomultiplier (PMA, Picoquant). The emission centered at 550 nm was purified by a monochrometer (SpectroPro 2300i, Princeton Instrument). The PL decay dynamics were achieved by a time-correlated single photon counting module (TCSPC Picoharp 300, Picoquant).

2.5. Electrochemical measurements

The electrochemical properties of the HCNs were investigated in a three-electrode configuration at 25 °C using saturated calomel electrode (SCE) as the reference electrode and Pt foil as the counter electrode in aqueous 6 M KOH electrolyte. The working electrode was prepared by mixing 80 wt% HCNs, 10 wt% carbon black (XC-72) and 10 wt% polyvinylidene fluoride (PVDF) using ethanol to produce a homogeneous paste. The paste was then coated onto nickel foam and dried overnight at 60 °C. All electrochemical measurements (cyclic voltammetry (CV) and galvanostatic charge discharge (GCD)) were conducted on a CHI 660E electrochemical workstation. The CVs curves were obtained between -0.2 V to -0.8 V potential window at scan rates of 10, 20, 30, 40, 50, 75 and 100 mV s⁻¹. The GCD was acquired between -0.2 V to -0.8 V at current densities of 1, 2, 4, 8 and 10 A g⁻¹. The cycling stability test was performed by galvanostatically charging and discharging for 10000 consecutive cycles at 4 A g⁻¹.

2.6. Photocatalytic degradation of VOCs

The volatile organic compounds (VOCs) degradation measurements were carried out with 1 mg of photocatalysts coated on a glass slide, using the drop-casting method. Quartz vials used for the VOCs adsorption and degradation were purged with concentration of approximately 2100 ppm for 1 min and 5 min respectively. The quartz vial reactors with the glass slides containing the photocatalysts were then illuminated by a light emitting diode (LED) with an intensity of 150 mW/cm² and a wavelength of 365 nm. The VOCs tested were ethanol, isopropyl alcohol (IPA) and methanol. 100 µl of the reaction mixture was extracted with a gas-tight syringe and injected into the gas chromatographer mass spectrometer (Shimadzu GCMS-QP2010 Ultra) at regular time intervals to determine the concentration of VOC remaining in the reactor.

3. Results and discussion

Uniform RF-resin spheres with an average size of 650 nm were synthesized via a hydrothermal process by the polymerization of resorcinol/formaldehyde in an ammonia/alcoholic environment. An understanding of activated carbon formation is established by investigating the morphology evolution with different amounts of KOH, as illustrated in Fig. 1a. Different amounts of KOH were introduced during the activation process with RF-resin:KOH mass ratios of 1:0, 1:1 and 1:1.5, and the resultant activated carbon obtained were labelled as carbon nanosphere (CN), porous carbon nanosphere (PCN) and hollow carbon nanosphere (HCN) respectively.

As seen in Fig. 1b, CNs exhibit a smooth surface and with the increase in KOH ratio, the surface of PCNs (Fig. 1c) was observed to be rougher, suggesting the formation of a porous framework due to the carbonization and activation process. Interestingly, when the KOH amount was increased further, the carbon retained its porous and spherical structure, but the simultaneous occurrence of exfoliation and excavation leaves the interior of the carbon hollow (Fig. 1d). The porous and hollow structures of HCNs are favorable for enhanced VOCs adsorptions and supercapacitance performances. The hierarchical porous structures aids in the adsorption and diffusivity of VOCs, enabling faster VOCs adsorption rate [12]. Also, due to the unique hollow structure, diffusion properties are suggested to be enhanced as a result of lower transport resistance [16]. Likewise for supercapacitance, the porous channels allows faster mass diffusion and transport, providing a

shorter diffusion pathway for high supercapacitance performance [19,30] while the hollow interior provides more accessible reactive sites in capacitive process to facilitate ion diffusion [20,31]. In addition, the surface and interior morphologies were further characterized by the FTIR, TEM and BET as structural properties such as surface chemistry, pore size, surface area, and architecture of activated carbons also play critical roles in enhancing VOCs adsorption capabilities and supercapacitance performances.

XRD pattern of various types of carbons obtained in Fig. 2a indicate the presence of graphitized carbon in the spherical structure. All samples had the same peaks that correspond to the (002) and (100) planes of graphitic carbon where θ is approximately 25° and 43° respectively [21]. Raman spectroscopy was also conducted as shown in Fig. 2b. All three samples clearly show the presence of the broad D and G bands at around 1350 and 1590 cm⁻¹ respectively [21,32]. The D peak corresponds to the disorder-induced defects of graphitic carbon, while the G band is associated with the presence of sp²-hybridized carbon in carbon materials [21,32]. The intensity ratio of I_D to I_G (I_D/I_G) of CNs and PCNs are 0.99 and 0.922 respectively, suggesting that lesser defects are formed with increased amounts of KOH. The I_D/I_G of HCNs is 1.93 (Fig. 2b), which is much higher than that of CNs and PCNs. However, it is noted that when the I_D/I_G ratio is above the value of 1.1, the increase in I_D/I_G is attributed to the increase in the number of graphite crystallites with lesser defects [33]. Therefore, the Raman spectra suggest that the number of defects and disorderness is reduced with increasing KOH concentrations.

As the oxygen surface functional groups are able to enhance polar molecules adsorptions [15] as well as increasing the rate capability of carbon material [34], different carbon spheres were analyzed using FTIR spectroscopy as shown in Fig. 2c. All spectrums reveal absorption bands at about 3400 cm⁻¹, 1630 cm⁻¹ and 1100 cm⁻¹ to 1250 cm⁻¹ which correspond to the OH hydroxyl functional groups, the skeletal vibration of aromatic C=C and C—O stretching vibrations respectively [6,22]. A slight decrease in the adsorption intensity can be observed for the OH groups with increasing KOH ratio. This could be due to the removal of H₂O during the activation process. Furthermore, the intensities of C=C and C—O bands also weaken slightly with KOH addition.

The hierarchical pore structure also plays an important role in both VOCs adsorption and supercapacitance, TEM image in Fig. 2d shows smooth spheres with little or no porosity as seen in the corresponding HRTEM image (Fig. 2g). After KOH activation, the surface of PCNs was

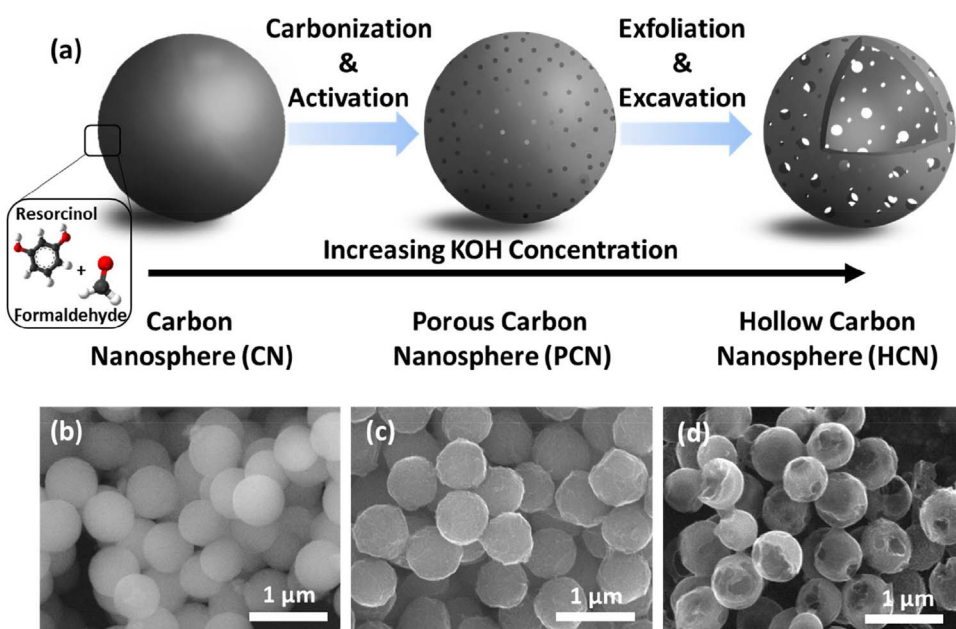


Fig. 1. (a) Schematic diagram illustrating synthesis process of CN, PCN and HCN by varying amounts of KOH. SEM images of (b) CNs, (c) PCNs, and (d) HCNs.

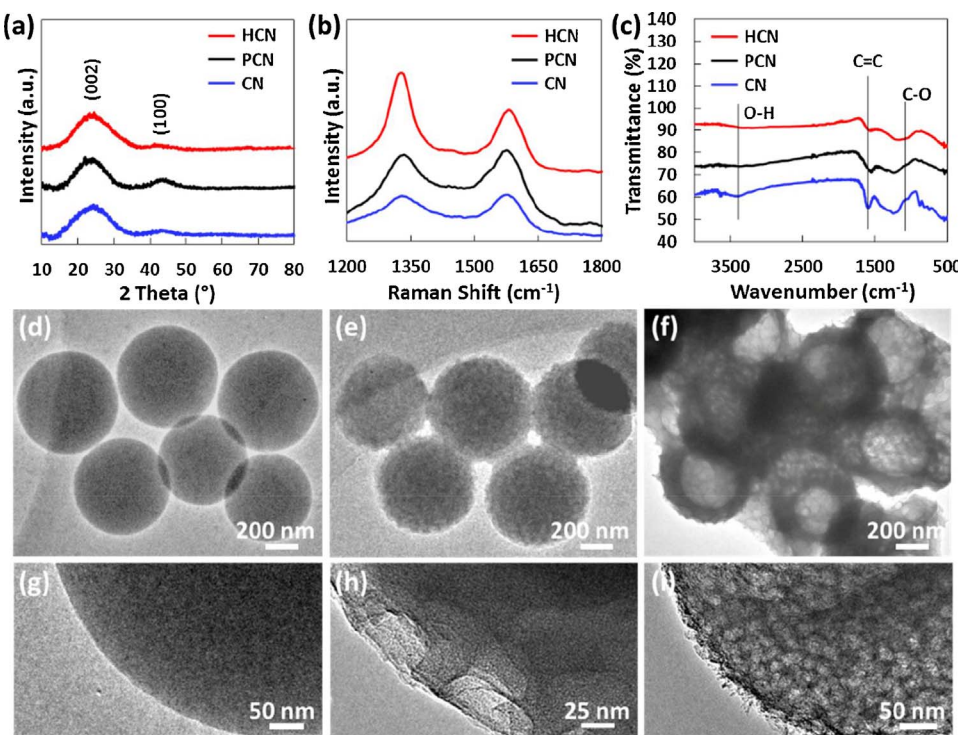


Fig. 2. (a) XRD pattern. (b) Raman spectra. (c) FTIR spectra of CN, PCN and HCN. TEM images of (d) CN (e) PCN (f) HCN. HRTEM image of (g) CN (h) PCN (i) HCN.

observed to be rougher, and the surface seemed to be exfoliated into thin sheets (Fig. 2e). The pores on the thinly exfoliated sheets on the surface of the PCNs appeared to be microporous as shown in the higher magnification TEM (Fig. 2h). In addition to the microporosity, an increased amount of exfoliated sheets and a hollow interior were observed in HCNs (Fig. 2f). Uniform mesopores can also be seen in the HCNs as shown in Fig. 2i, which are likely formed due to the pore widening effect [11] with the increased amounts of KOH used.

To understand the formation of micropores and mesopores caused by the increased amounts of KOH, Brunauer–Emmett–Teller (BET) analysis was conducted. The specific surface areas (S_{BET}), pore volumes and average pore sizes are summarized in Table 1. Fig. 3a reveals that both CNs and PCNs exhibits type-I isotherm, indicating the presence of only micropores in the nanostructures. The difference in surface area observed for both samples is most likely due to the increase in the number of micropores in PCNs, as a result of the etching of KOH. PCNs have a S_{BET} of $1159 \text{ m}^2 \text{ g}^{-1}$ while CNs only exhibit a S_{BET} of $477 \text{ m}^2 \text{ g}^{-1}$. Furthermore, Table 1 reveals an increase in the total pore volume of PCNs ($V_t = 0.479 \text{ cm}^3 \text{ g}^{-1}$) as compared to CNs ($V_t = 0.213 \text{ cm}^3 \text{ g}^{-1}$), where the increase in total pore volume is mostly attributed to the increase in micropores volume (V_{micro}) from $0.19 \text{ cm}^3 \text{ g}^{-1}$ to $0.45 \text{ cm}^3 \text{ g}^{-1}$. HCNs exhibited type-IV isotherms with a hysteresis loop, suggesting the presence of mesopores. Fig. 3b shows an increase in microporous pore size distribution as well as a broad peak in larger pore diameter region, indicating the existence of mesopores in HCNs and suggesting a hierarchical pore structure. HCNs has the highest S_{BET} of $1227 \text{ m}^2 \text{ g}^{-1}$ as compared to PCNs and CNs. The

micropores and mesopores volume ($V_{\text{micro}} = 0.81 \text{ cm}^3 \text{ g}^{-1}$, $V_{\text{meso}} = 0.095 \text{ cm}^3 \text{ g}^{-1}$) also increased with more KOH activation. Based on the above results, the formation of micropores and mesopores become more obvious with increasing KOH addition. A 3D hierarchical porous carbon (HCNs) with micro and mesopores can thus be synthesized with a simple one-step KOH activation process. The VOCs adsorption of these activated carbons were investigated. It was observed that HCNs exhibited the best performance in ethanol adsorption (Fig. 3c), with only 74% of ethanol remaining in the environment, while CNs and PCNs demonstrated poorer adsorption with 83% and 80% remaining respectively. The adsorption tests were also carried out with other VOCs such as IPA and methanol. The results at 50 min interval for all VOCs were summarized as shown in Fig. 3d. The individual adsorption kinetics plot with time evolution for IPA and methanol can be found in the Supplementary Information (Fig. S1). For IPA, CNs still performs the worst with 88% of IPA remaining, while PCNs and HCNs had 75% and 72% respectively. Lastly, methanol adsorption for CNs had 95% remaining, followed by 96% and 89% for PCNs and HCNs respectively. It is apparent that CNs has more oxygen surface functional groups (Fig. 2c) as compared to PCNs and HCNs which should suggests higher VOCs adsorption amounts. However, the adsorptions of polar VOCs molecules follow an inverse trend to the intensity of the functional groups. This suggests that the enhanced adsorption of the three VOCs in HCNs are more likely to be attributed to the increase in micropores for VOCs containment as well as the mesoporous pore structures which allow easy accessibility for larger VOCs molecules [12,35]. The fast adsorption of ethanol within 20 min

Table 1
Specific surface areas, pore volumes, and average pore sizes of CNs, PCNs and HCNs.

Sample	$S_{\text{BET}}^{\text{a}} [\text{m}^2 \text{ g}^{-1}]$	$V_{\text{micro}}^{\text{b}} [\text{cm}^3 \text{ g}^{-1}]$	$V_{\text{meso}} [\text{cm}^3 \text{ g}^{-1}]$	$V_t^{\text{c}} [\text{cm}^3 \text{ g}^{-1}]$	$\text{Ratio}_{\text{micro}} [\%]$	Average pore size [nm]
CN	477	0.19	0.023	0.213	89.2	0.89
PCN	1159	0.45	0.029	0.479	93.9	0.85
HCN	1227	0.81	0.095	0.905	89.5	1.44

^a Surface area was calculated using the BET method at $P/P_0 = 0.01\text{--}0.1$.

^b Evaluated by Quenched Solid Density Functional Theory (QSDFT) method.

^c Total pore volume at $P/P_0 = 0.99$.

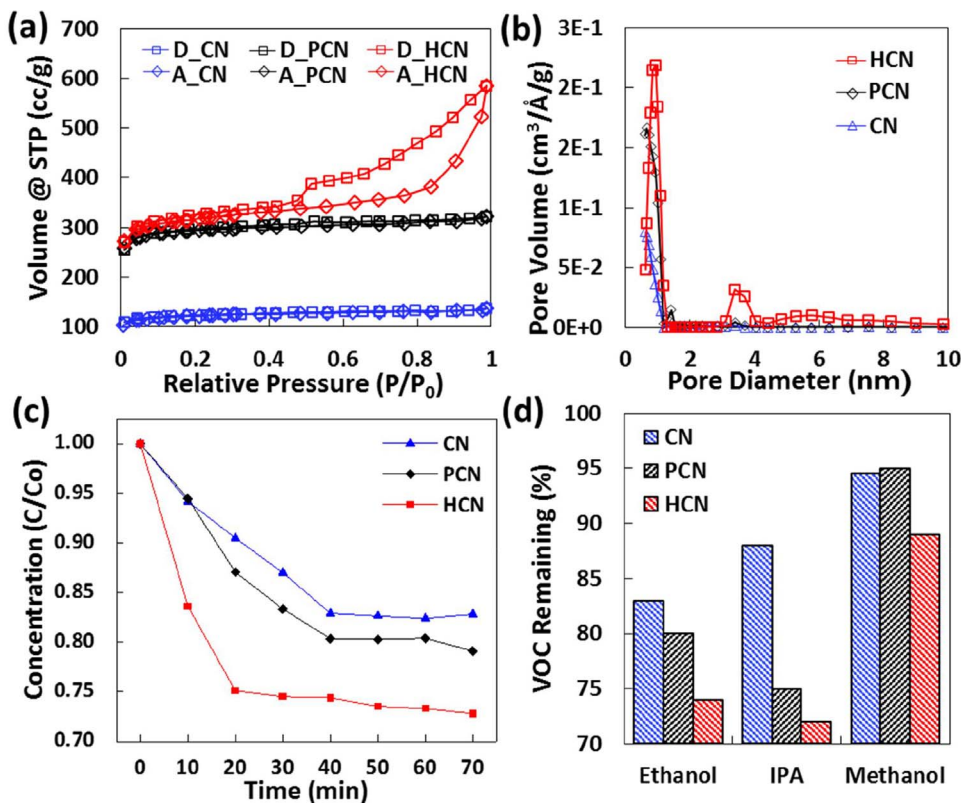


(Fig. 3c) is likely due to the regularly shaped mesopores structure (Fig. 2i). Having a regularly shaped structure provides an advantage in decreasing the diffusion resistance of adsorbate molecules [12,18], taking a shorter time to reach equilibrium (Fig. 3c). Moreover, the hollow interior leads to a high surface to volume ratio, creating more active sites for VOCs adsorption. The above results reveal that the fast and enhanced VOCs adsorptions are highly dependent on the hollow and hierarchical pore structures of the carbon spheres.

Besides that, carbonaceous materials possessing large accessible surface areas have been recognized as promising supercapacitor electrode materials due to remarkable electrical double-layer capacitive performances. 3D porous carbons are known to be ideal materials for supercapacitor applications due to the existence of micropores for high energy storage [7], mesopores for the acceleration of ion diffusion in the electrodes [36] and macropores due to the hollow interior serving as ion-buffering reservoirs [36].

Since HCNs exhibited characteristics of a hierarchical porous carbon and possesses the highest S_{BET} out of the three carbon materials, the capacitive properties of the as-prepared HCNs were studied by cyclic voltammetry (CV) and galvanostatic charge-discharge (GCD) measurements using a conventional three-electrode system with saturated calomel electrode (SCE) as the reference electrode and Pt foil as the counter electrode in aqueous 6 M KOH electrolyte solution. Fig. 4a shows the CV curves of the HCNs electrode at various scan rates from 10 to 100 mV s⁻¹ in the potential window from -0.2 to -0.8 V. The quasi-rectangular and symmetric shape of the CV curves without any redox peaks indicate that capacitive properties of HCNs are governed by the pure electrical double-layer capacitance (EDLC) characteristics. Moreover, the shape of the curves remained almost unchanged even at high scan rates (75 mV s⁻¹ and 100 mV s⁻¹), indicating good rate capability of the HCNs against rapid charging-discharging. To further examine the electrochemical properties, GCD measurements were performed at various current densities from 1 to 10 A g⁻¹ (Fig. 4b). The symmetric triangular shapes of the GCD curves confirm the sole capacitive contribution from the EDLC characteristics of the HCNs. Based on

Fig. 3. (a) N₂ adsorption-desorption isotherm and (b) pore size distribution curves of CN, PCN and HCN. Adsorption kinetics of (c) ethanol with time evolution and (d) various VOCs at 50 min.

the GCD curves, the specific capacitance values were calculated using the following equation:

$$C_s = \frac{I \times \Delta t_d}{\Delta V_d}$$

where I is the discharge current density (A g⁻¹), Δt_d is the discharge time (s) and ΔV_d is the voltage drop (V) upon discharging. As shown in Fig. 4c, the HCNs exhibited a specific capacitance of 353 F g⁻¹ at 1 A g⁻¹. When the current density was increased to 2, 4, 8, and 10 A g⁻¹, high specific capacitances of 342, 336, 326 and 320 F g⁻¹ were still achieved, respectively. About 90% of the specific capacitance was retained when the current density increased from 1 A g⁻¹ to 10 A g⁻¹, demonstrating excellent rate capability of the HCNs. Notably, the specific capacitance of HCNs is comparable or even superior than the recently reported carbonaceous materials, such as fibrous-structured hollow mesoporous carbon spheres (359.2 F g⁻¹ at 1 A g⁻¹) [37], KOH activated ordered mesoporous carbons (200 F g⁻¹ at 0.5 A g⁻¹) [38], nitrogen-enriched nanocarbons (325 F g⁻¹ at 0.1 A g⁻¹) [39], hierarchical porous carbon hollow-spheres with micropore shells and meso/macropore cores (270 F g⁻¹ at 0.5 A g⁻¹) [40], polymerization-activated hierarchical porous carbon membrane (297 F g⁻¹ at 0.5 A g⁻¹) [41], hollow porous carbon spheres with micro/mesoporous combination shell and macroporous core (303.9 F g⁻¹ at 1 A g⁻¹) [42] and hierarchically porous carbon spheres prepared by emulsification-crosslinking method (328 F g⁻¹ at 0.5 A g⁻¹) [43]. Apart from the capacitive properties of the electrode materials, another critical evaluation parameter of the supercapacitor electrodes is the cycle life after multiple consecutive charge-discharge cycling process. The cycling stability test was performed by continuous charge-discharge cycling of the HCNs electrode between -0.2 V to -0.8 V at a current density of 4 A g⁻¹ for 10,000 cycles. Fig. 4d shows the capacitance retention as a function of cycle number. The HCNs electrode exhibits an impressive electrochemical stability with only 3.2% capacitance loss after 10,000 cycles, which can be clearly confirmed by the last 10 cycles (inset of Fig. 4d). The excellent performance of the HCNs electrode is closely

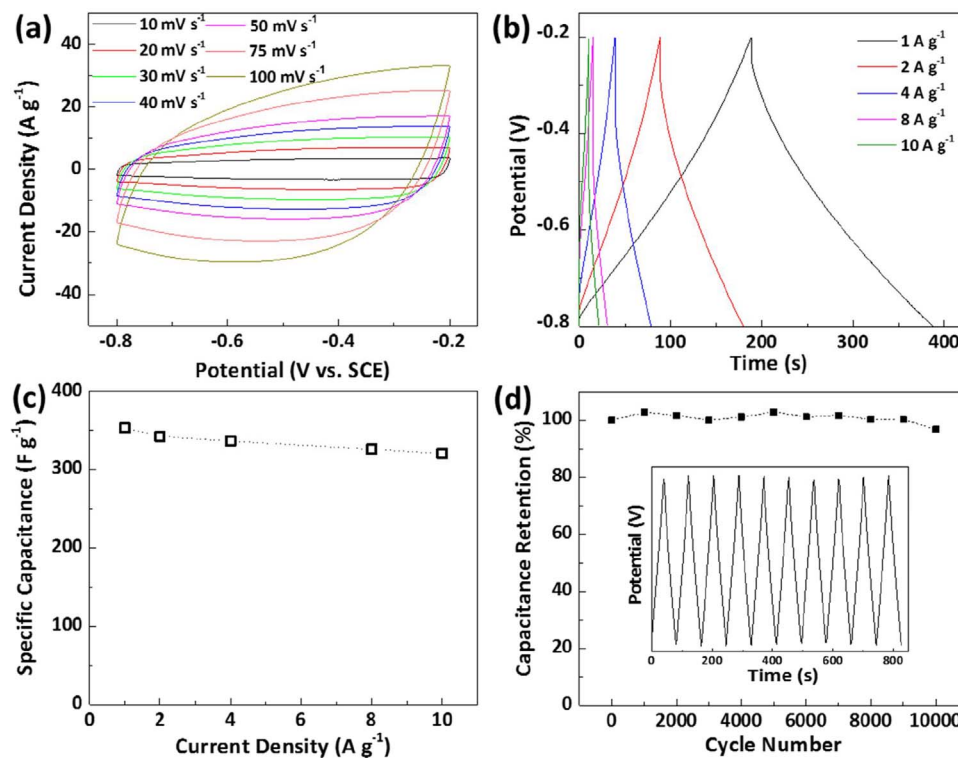


Fig. 4. (a) Cyclic voltammetry (CV) curves of HCNs at scan rates of 10, 20, 30, 40, 50, 75 and 100 mV s^{-1} . (b) Galvanostatic charge-discharge (GCD) profiles obtained at current densities of 1, 2, 4, 8 and 10 A g^{-1} . (c) Corresponding specific capacitance values calculated at specified current densities. (d) Cycling performance for the HCNs at a current density of 4 A g^{-1} over 10000 cycles. The inset shows the last ten cycles.

related to the rational engineering of the carbon nanospheres towards conductive porous nanostructures with hollow interior. The electrochemical impedance spectroscopy (EIS) measurement was carried out for CNs, PCNs and HCNs. The semicircle of the HCNs is the smallest and has a nearly vertical line which clearly demonstrates the superior conductivity of the carbon material, supporting the high electrochemical performance of the HCNs (Fig. S2). This structure introduces abundant electroactive sites, which can be easily and rapidly accessed by electrolyte ions through porous channels that offer shorter diffusion pathways [19]. Moreover, the hollow interior can effectively accommodate large number of ions during progressive ion diffusion with high rate, thus increasing rate capability of the electrode [20].

In addition to the VOC adsorption and supercapacitor capabilities, TiO_2 sheets were hydrothermally grown on the HCNs and tested for its degradation performance. The uniformity of HCNs allows the easy growth of TiO_2 sheets on the HCNs. Fig. 5a shows the SEM image of TiO_2 conformably coated on the HCNs, while the inset shows a high magnification image of an exposed HCN core with TiO_2 sheets on the outer surface. The TEM image in Fig. 5b also shows the presence of thin layered sheets on the outer surface of the HCNs. However, due to the size of HCN@ TiO_2 which is approximately 800 nm in diameter, the TEM is unable to clearly portray the hollow carbon core inside the TiO_2 sheets. As such, the presence of the HCN core will be ascertained by other characterization tools. The elemental mapping in Fig. 5c further confirms the presence of the HCNs and TiO_2 sheets. It is evident that the core of the HCN@ TiO_2 is made up of C, while the outer shell consists of Ti and O elements. The sample is further characterized with XRD and the diffraction pattern (Fig. 5d) reveals the high anatase crystallinity of TiO_2 after annealing at 450 °C for 2 h. The TiO_2 anatase diffraction peaks are in good agreement with the literature reports (JCPDS no. 21–1272). The graph in Fig. 5d also shows that the graphitic carbon peak at 25° was present despite the hydrothermal treatment as well as the post annealing process for TiO_2 , indicating that the HCN core remained. Furthermore, the HRTEM image in Fig. 5e shows the adjacent lattice spacing of 0.35 nm attributed to the (101) plane, and lattice spacing of 0.236 nm attributed to the (004) plane of TiO_2 . Both lattice spacings observed also correspond to the XRD spectra in Fig. 5d. An

SEM EDX spectrum (Fig. 5f) was also obtained to indicate the presence of Ti, O and C elements in the HCN@ TiO_2 sample. The Si peak observed is due to the Si substrate that was used while imaging the sample.

CN@ TiO_2 and HCN@ TiO_2 were tested for their VOC photodegradation performance. Fig. 6a shows that HCN@ TiO_2 degrades ethanol faster than CN@ TiO_2 as indicated by the drop in ethanol concentration to 22% and 71% respectively. The degradation of other VOCs such as IPA and methanol were also investigated. The concentration at 60 min mark for all VOCs were summarized in Fig. 6b. The individual degradation kinetics with time evolution plots for IPA and methanol can be found in the Supplementary Information (Fig. S3). At 60 min, CN@ TiO_2 shows a degradation of up to 59% while HCN@ TiO_2 has almost completely degraded IPA showing a concentration of 1% remaining. Methanol degradation follows the same trend where HCN@ TiO_2 performed better than CN@ TiO_2 . Stability of the HCN@ TiO_2 has also been demonstrated as shown in Fig. S4. It was noted that the performances for three different VOCs (ethanol, IPA and methanol) were consistent over 4 cycles, indicating a stable photodegradation activity for HCN@ TiO_2 .

The excellent performance can be ascribed to two reasons: (i) The high surface area of HCNs which leads to an increase in the number of abundant active sites, assisting in adsorbing and containing the VOCs. These contained VOCs are then degraded by the TiO_2 grown on HCNs. (ii) The graphitization and lesser defects in HCNs may allow better charge transfer of the electrons from TiO_2 to HCN, leaving more holes behind to react with adsorb H_2O to form hydroxyl radical [44], which then react with the VOCs and thus, enhancing the VOCs degradation rate. To further understand the charge transfer mechanism, photoluminescence (PL) measurement was employed to analyze the efficiency of the transfer and migration of electrons of the HCN@ TiO_2 photocatalyst.

Photoluminescence (PL) emission arises from the recombination of free carriers [45,46] and the intensity of PL emission reflects the efficiency of the charge transfer process. The excitation wavelength used is 350 nm and it is observed that both samples exhibited a peak at around 540 nm to 550 nm (Fig. 6c). This peak may be attributed to the transition from oxygen vacancies with one trapped electron to the valence

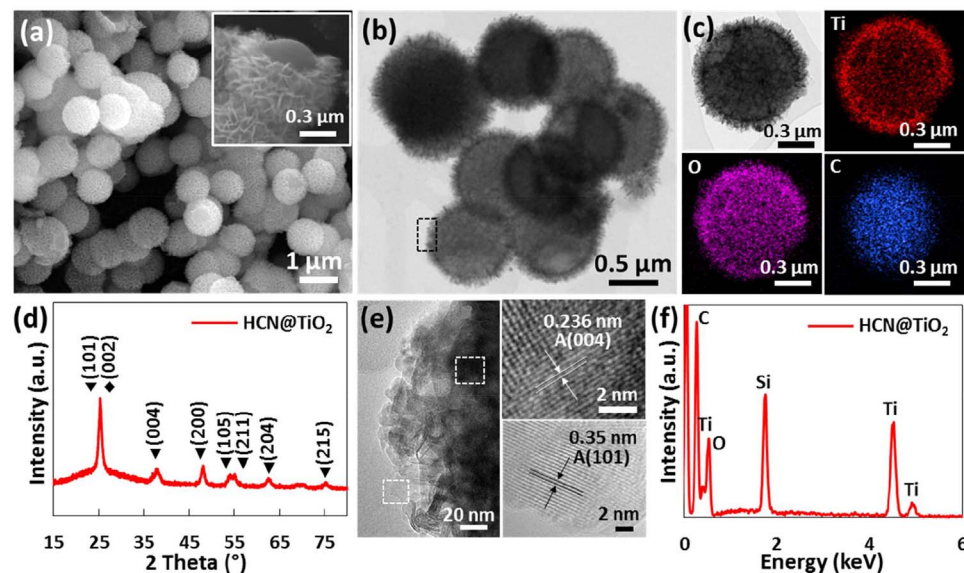


Fig. 5. (a) SEM image and high magnification SEM image (inset) of HCN@TiO₂ (b) TEM image of HCN@TiO₂ (c) TEM image and element mapping of Ti, O and C. (d) XRD Spectra of HCN @TiO₂ (e) High magnification TEM and HRTEM image of HCN@TiO₂ and (f) EDX Spectra of HCN@TiO₂.

band of TiO₂ [47]. A suppressed peak was observed in HCN@TiO₂ as compared to CN@TiO₂. The drop in PL intensity indicates the reduced recombination of photoinduced electron-hole pairs [48] in the less defective HCN@TiO₂ (Fig. 2b), suggesting a higher charge transfer efficiency which leads to an enhancement in the VOCs photodegradation performance. The suppression of PL also imply a faster charge transfer process with a shorter decay lifetime for the photoinduced electrons [49–51]. As such, this phenomenon is further investigated using the time-resolved transient PL. The emission decay curves of both samples (Fig. 6d) are fitted by exponential kinetics function where three lifetime values were derived. The equations used for the fitting and calculations of the average lifetime τ_A are shown below.

$$I(t) = A_1 \exp(-t/\tau_1) + A_2 \exp(-t/\tau_2) + A_3 \exp(-t/\tau_3) \quad (1)$$

$$\tau_A = \frac{A_1 \tau_1^2 + A_2 \tau_2^2 + A_3 \tau_3^2}{A_1 \tau_1 + A_2 \tau_2 + A_3 \tau_3} \quad (2)$$

The values obtained for emission lifetime τ_1 , τ_2 and τ_3 and its respective amplitudes (A_1 , A_2 and A_3) are reflected in Table 2. The average emission lifetime which reflects the overall emission decay behaviour of sample were calculated and show that HCN@TiO₂ has a

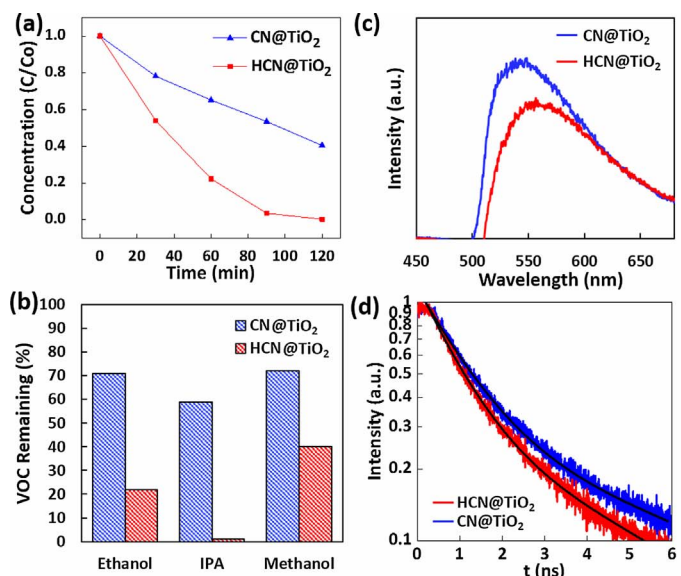
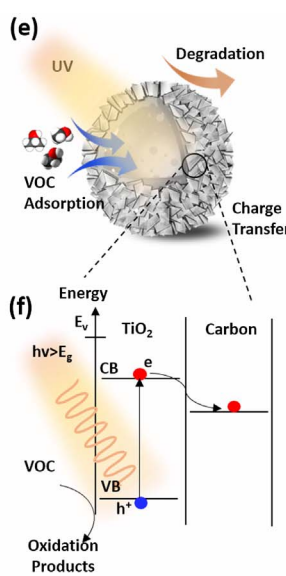


Fig. 6. VOC degradation with time evolution (a) ethanol and (b) various VOCs at 60 min (c) Photoluminescence spectra and (d) time-resolved transient photoluminescence (PL) decay (excitation at 350 nm) of CN@TiO₂ and HCN@TiO₂. (e) Schematic diagram of VOC adsorption and degradation (f) Mechanism of charge transfer of HCN@TiO₂.



leaving behind more holes in TiO₂ for reaction with VOCs (Fig. 6f). This prevents recombination of electron-hole pair [52], which leads to a suppressed PL peak of HCN@TiO₂ as compared to CN@TiO₂. This mechanism provides the capability for enhanced VOCs degradation due to efficient charge transfer.

4. Conclusion

Hollow and hierarchical porous carbon has been synthesized by a simple one-step KOH chemical activation process for enhanced pollutant adsorption and energy storage. The pore size distribution of the carbon can be easily tuned by variation in KOH amounts to simultaneously obtain micropores, mesopores and a hollow structure (macropores). In addition, HCNs has exhibited a high surface area of 1227 m² g⁻¹ through the KOH activation. The synthesized HCNs revealed superior VOCs adsorption as compared to CNs and PCNs due to presences of micro and mesopores, which contain and increase selectivity of adsorption of larger VOCs molecules respectively, while the hollow interior (macropores) promotes transport diffusion of VOCs. Furthermore, supercapacitance measurements has also shown high capacitive performance of 353 F g⁻¹ and excellent stability of only 3.2% capacitance loss after 10000 cycles. The high performance is attributed to the rational engineering of the carbon nanospheres towards hierarchical porous structures with hollow cavity. TiO₂ nanosheets has also been grown on the above mentioned carbon leading to improved photocatalytic degradation. Such designed KOH activated carbon with hollow and hierarchical pores structure can be effortlessly obtained under variation in KOH amounts, which enhances the removal of VOCs and supercapacitive performances, providing a cleaner indoor environment and highly favourable supercapacitance system.

Acknowledgements

This research is supported by the National Research Foundation (NRF), under Energy Innovation Research Programme (EIRP) R-263-000-B82-279, managed on behalf of Building and Construction Authority (BCA).

Appendix A. Supplementary data

Supplementary data associated with this article can be found, in the online version, at <http://dx.doi.org/10.1016/j.apcatb.2017.08.069>.

References

- [1] S. Li, C. Cheng, A. Thomas, Carbon-Based microbial-fuel-cell electrodes: from conductive supports to active catalysts, *Adv. Mater.* 29 (2017) 1602547 (n/a).
- [2] Q. Ma, Y. Yu, M. Sindoro, A.G. Fane, R. Wang, H. Zhang, Carbon-based functional materials derived from waste for water remediation and energy storage, *Adv. Mater.* 29 (2017) 1605361-n/a.
- [3] K.J. Lee, J. Miyawaki, N. Shiratori, S.-H. Yoon, J. Jang, Toward an effective adsorbent for polar pollutants: formaldehyde adsorption by activated carbon, *J. Hazard. Mater.* 260 (2013) 82–88.
- [4] A. Veksha, E. Sasaoka, M.A. Uddin, The influence of porosity and surface oxygen groups of peat-based activated carbons on benzene adsorption from dry and humid air, *Carbon* 47 (2009) 2371–2378.
- [5] M. Li, F. Xu, H. Li, Y. Wang, Nitrogen-doped porous carbon materials: promising catalysts or catalyst supports for heterogeneous hydrogenation and oxidation, *Catal. Sci. Technol.* 6 (2016) 3670–3693.
- [6] M. Li, C. Liu, H. Cao, H. Zhao, Y. Zhang, Z. Fan, KOH self-templating synthesis of three-dimensional hierarchical porous carbon materials for high performance supercapacitors, *J. Mater. Chem. A* 2 (2014) 14844–14851.
- [7] X. Yu, J. Zhao, R. Lv, Q. Liang, C. Zhan, Y. Bai, Z.-H. Huang, W. Shen, F. Kang, Facile synthesis of nitrogen-doped carbon nanosheets with hierarchical porosity for high performance supercapacitors and lithium-sulfur batteries, *J. Mater. Chem. A* 3 (2015) 18400–18405.
- [8] W. Zhang, H. Huang, F. Li, K. Deng, X. Wang, Palladium nanoparticles supported on graphitic carbon nitride-modified reduced graphene oxide as highly efficient catalysts for formic acid and methanol electrooxidation, *J. Mater. Chem. A* 2 (2014) 19084–19094.
- [9] W. Zhang, Q. Yao, X. Wu, Y. Fu, K. Deng, X. Wang, Intimately coupled hybrid of graphitic carbon nitride nanoflakelets with reduced graphene oxide for supporting Pd nanoparticles: a stable nanocatalyst with high catalytic activity towards formic acid and methanol electrooxidation, *Electrochim. Acta* 200 (2016) 131–141.
- [10] W. Zhang, Y. Fu, J. Wang, X. Wang, 3D hierarchically porous graphitic carbon nitride modified graphene-Pt hybrid as efficient methanol oxidation catalysts, *Adv. Mater. Interfaces* 4 (2017) 1601219-n/a.
- [11] J. Wang, S. Kaskel, KOH activation of carbon-based materials for energy storage, *J. Mater. Chem.* 22 (2012) 23710–23725.
- [12] G. Wang, B. Dou, Z. Zhang, J. Wang, H. Liu, Z. Hao, Adsorption of benzene, cyclohexane and hexane on ordered mesoporous carbon, *J. Environ. Sci.* 30 (2015) 65–73.
- [13] S.M. de Arruda, Guelli Ulson de Souza, A.D. da Luz, A. da Silva, A.A. Ulson de Souza, Removal of mono- and multicomponent BTX compounds from effluents using activated carbon from coconut shell as the adsorbent, *Ind. Eng. Chem. Res.* 51 (2012) 6461–6469.
- [14] M.A. Lillo-Ródenas, D. Cazorla-Amorós, A. Linare-Solano, Behaviour of activated carbons with different pore size distributions and surface oxygen groups for benzene and toluene adsorption at low concentrations, *Carbon* 43 (2005) 1758–1767.
- [15] A. Silvestre-Albero, J. Silvestre-Albero, A. Sepúlveda-Escribano, F. Rodríguez-Reinozo, Ethanol removal using activated carbon: effect of porous structure and surface chemistry, *Microporous Mesoporous Mater.* 120 (2009) 62–68.
- [16] X. He, H. Sun, M. Zhu, M. Yaseen, D. Liao, X. Cui, H. Guan, Z. Tong, Z. Zhao, N-doped porous graphitic carbon with multi-flaky shell hollow structure prepared using a green and ‘useful’ template of CaCO₃ for VOC fast adsorption and small peptide enrichment, *Chem. Commun.* 53 (2017) 3442–3445.
- [17] Q. Li, N. Chen, X. Xing, X. Xiao, Y. Wang, I. Djerdj, NiO nanosheets assembled into hollow microspheres for highly sensitive and fast-responding VOC sensors, *RSC Adv.* 5 (2015) 80786–80792.
- [18] L. Ji, F. Liu, Z. Xu, S. Zheng, D. Zhu, Adsorption of pharmaceutical antibiotics on template-synthesized ordered micro- and mesoporous carbons, *Environ. Sci. Technol.* 44 (2010) 3116–3122.
- [19] S.L. Candelaria, Y. Shao, W. Zhou, X. Li, J. Xiao, J.-G. Zhang, Y. Wang, J. Liu, J. Li, G. Cao, Nanostructured carbon for energy storage and conversion, *Nano Energy* 1 (2012) 195–220.
- [20] X.-Y. Yu, L. Yu, X.W. Lou, Metal sulfide hollow nanostructures for electrochemical energy storage, *Adv. Energy Mater.* 6 (2016) 1501333-n/a.
- [21] X. Zheng, W. Lv, Y. Tao, J. Shao, C. Zhang, D. Liu, J. Luo, D.-W. Wang, Q.-H. Yang, Oriented and interlinked porous carbon nanosheets with an extraordinary capacitive performance, *Chem. Mater.* 26 (2014) 6896–6903.
- [22] Y. Wang, B. Chang, D. Guan, X. Dong, Mesoporous activated carbon spheres derived from resorcinol-formaldehyde resin with high performance for supercapacitors, *J. Solid State Electrochem.* 19 (2015) 1783–1791.
- [23] Y. Li, X. Zhang, R. Yang, G. Li, C. Hu, The role of H₃PO₄ in the preparation of activated carbon from NaOH-treated rice husk residue, *RSC Adv.* 5 (2015) 32626–32636.
- [24] A. Chen, Y. Yu, H. Lv, Y. Wang, S. Shen, Y. Hu, B. Li, Y. Zhang, J. Zhang, Thin-walled, mesoporous and nitrogen-doped hollow carbon spheres using ionic liquids as precursors, *J. Mater. Chem. A* 1 (2013) 1045–1047.
- [25] X. Fang, J. Zang, X. Wang, M.-S. Zheng, N. Zheng, A multiple coating route to hollow carbon spheres with foam-like shells and their applications in supercapacitor and confined catalysis, *J. Mater. Chem. A* 2 (2014) 6191–6197.
- [26] G.A. Ferrero, A.B. Fuertes, M. Sevilla, N-doped porous carbon capsules with tunable porosity for high-performance supercapacitors, *J. Mater. Chem. A* 3 (2015) 2914–2923.
- [27] F.-L. Wang, L.-L. Pang, Y.-Y. Jiang, B. Chen, D. Lin, N. Lun, H.-L. Zhu, R. Liu, X.-L. Meng, Y. Wang, Y.-J. Bai, L.-W. Yin, Simple synthesis of hollow carbon spheres from glucose, *Mater. Lett.* 63 (2009) 2564–2566.
- [28] X. Sun, Y. Li, Hollow carbonaceous capsules from glucose solution, *J. Colloid Interface Sci.* 291 (2005) 7–12.
- [29] Z. Wen, Q. Wang, Q. Zhang, J. Li, Hollow carbon spheres with wide size distribution as anode catalyst support for direct methanol fuel cells, *Electrochim. Commun.* 9 (2007) 1867–1872.
- [30] B. You, J. Yang, Y. Sun, Q. Su, Easy synthesis of hollow core, bimodal mesoporous shell carbon nanospheres and their application in supercapacitor, *Chem. Commun.* 47 (2011) 12364–12366.
- [31] T. Zhu, L. Zhu, J. Wang, G.W. Ho, Rational integration of inbuilt aperture with mesoporous framework in unusual asymmetrical yolk-shell structures for energy storage and conversion, *ACS Appl. Mater. Interfaces* 8 (2016) 32901–32909.
- [32] B. Chen, R. Li, G. Ma, X. Gou, Y. Zhu, Y. Xia, Cobalt sulfide/N,S codoped porous carbon core-shell nanocomposites as superior bifunctional electrocatalysts for oxygen reduction and evolution reactions, *Nanoscale* 7 (2015) 20674–20684.
- [33] N.H. Cho, D.K. Veirs, J.W. Ager III, M.D. Rubin, C.B. Hopper, D.B. Bogy, Effects of substrate temperature on chemical structure of amorphous carbon films, *J. Appl. Phys.* 71 (1992) 2243–2248.
- [34] K. Zhu, Y. Wang, J.A. Tang, S. Guo, Z. Gao, Y. Wei, G. Chen, Y. Gao, A high-performance supercapacitor based on activated carbon fibers with an optimized pore structure and oxygen-containing functional groups, *Mater. Chem. Front.* 1 (2017) 958–966.
- [35] B. Dou, Q. Hu, J. Li, S. Qiao, Z. Hao, Adsorption performance of VOCs in ordered mesoporous silicas with different pore structures and surface chemistry, *J. Hazard. Mater.* 186 (2011) 1615–1624.
- [36] H. Jiang, P.S. Lee, C. Li, 3D carbon based nanostructures for advanced supercapacitors, *Energy Environ. Sci.* 6 (2013) 41–53.
- [37] Q. Zhang, L. Li, Y. Wang, Y. Chen, F. He, S. Gai, P. Yang, Uniform fibrous-structured hollow mesoporous carbon spheres for high-performance supercapacitor electrodes, *Electrochim. Acta* 176 (2015) 542–547.
- [38] Y. Lv, F. Zhang, Y. Dou, Y. Zhai, J. Wang, H. Liu, Y. Xia, B. Tu, D. Zhao, A

- comprehensive study on KOH activation of ordered mesoporous carbons and their supercapacitor application, *J. Mater. Chem.* 22 (2012) 93–99.
- [39] X. Yang, C. Li, R. Fu, Nitrogen-enriched carbon with extremely high mesoporosity and tunable mesopore size for high-performance supercapacitors, *J. Power Sources* 319 (2016) 66–72.
- [40] Y. Han, X. Dong, C. Zhang, S. Liu, Hierarchical porous carbon hollow-spheres as a high performance electrical double-layer capacitor material, *J. Power Sources* 211 (2012) 92–96.
- [41] F. Ran, K. Shen, Y. Tan, B. Peng, S. Chen, W. Zhang, X. Niu, L. Kong, L. Kang, Activated hierarchical porous carbon as electrode membrane accommodated with triblock copolymer for supercapacitors, *J. Membr. Sci.* 514 (2016) 366–375.
- [42] J. Liu, X. Wang, J. Gao, Y. Zhang, Q. Lu, M. Liu, Hollow porous carbon spheres with hierarchical nanoarchitecture for application of the high performance supercapacitors, *Electrochim. Acta* 211 (2016) 183–192.
- [43] D. Zhang, J. Gao, Z. Li, S. He, J. Wang, Synthesis of hierarchically porous carbon spheres by an emulsification-crosslinking method and their application in supercapacitors, *RSC Adv.* 6 (2016) 54880–54888.
- [44] D.F. Ollis, E. Pelizzetti, N. Serpone, Photocatalyzed destruction of water contaminants, *Environ. Sci. Technol.* 25 (1991) 1522–1529.
- [45] Y. Dou, S. Zhang, T. Pan, S. Xu, A. Zhou, M. Pu, H. Yan, J. Han, M. Wei, D.G. Evans, X. Duan, TiO₂@Layered double hydroxide core-Shell nanospheres with largely enhanced photocatalytic activity toward O₂ generation, *Adv. Funct. Mater.* 25 (2015) 2243–2249.
- [46] J. Tian, Y. Sang, Z. Zhao, W. Zhou, D. Wang, X. Kang, H. Liu, J. Wang, S. Chen, H. Cai, H. Huang, Enhanced photocatalytic performances of CeO₂/TiO₂ nanobelts heterostructures, *Small* 9 (2013) 3864–3872.
- [47] E. Wang, T. He, L. Zhao, Y. Chen, Y. Cao, Improved visible light photocatalytic activity of titania doped with tin and nitrogen, *J. Mater. Chem.* 21 (2011) 144–150.
- [48] W. Zhou, H. Liu, J. Wang, D. Liu, G. Du, J. Cui, Ag₂O/TiO₂ nanobelts heterostructure with enhanced ultraviolet and visible photocatalytic activity, *ACS Appl. Mater. Interfaces* 2 (2010) 2385–2392.
- [49] H.B. Kim, I. Im, Y. Yoon, S.D. Sung, E. Kim, J. Kim, W.I. Lee, Enhancement of photovoltaic properties of CH₃NH₃PbBr₃ heterojunction solar cells by modifying mesoporous TiO₂ surfaces with carboxyl groups, *J. Mater. Chem. A* 3 (2015) 9264–9270.
- [50] Z. Zhang, Y. Huang, K. Liu, L. Guo, Q. Yuan, B. Dong, Multichannel-improved charge-carrier dynamics in well-designed hetero-nanostructural plasmonic photocatalysts toward highly efficient solar-to-fuels conversion, *Adv. Mater.* 27 (2015) 5906–5914.
- [51] M.-Q. Yang, Y.-J. Xu, W. Lu, K. Zeng, H. Zhu, Q.-H. Xu, G.W. Ho, Self-surface charge exfoliation and electrostatically coordinated 2D hetero-layered hybrids, *Nat. Commun.* 8 (2017) 14224.
- [52] R. Sellappan, A. Galekas, V. Venkatachalapathy, A.Y. Kuznetsov, D. Chakarov, On the mechanism of enhanced photocatalytic activity of composite TiO₂/carbon nanofilms, *Appl. Catal. B* 106 (2011) 337–342.